Photoionization of cold gas phase coronene and its clusters: Autoionization resonances in monomer, dimer, and trimer and electronic structure of monomer cation

Philippe Bréchignac, Gustavo A. Garcia, Cyril Falvo, Christine Joblin, Damian Kokkin, Anthony Bonnamy, Pascal Parneix, Thomas Pino, Olivier Pirali, Giacomo Mulas, and Laurent Nahon

Articles you may be interested in

Competitive fragmentation pathways of acetic acid dimer explored by synchrotron VUV photoionization mass spectrometry and electronic structure calculations
J. Chem. Phys. **137**, 124308 (2012); 10.1063/1.4754273

Zero kinetic energy photoelectron spectroscopy of tryptamine and the dissociation pathway of the singly hydrated cation cluster
J. Chem. Phys. **137**, 104312 (2012); 10.1063/1.4752080

Gas-phase structures of neutral silicon clusters
J. Chem. Phys. **136**, 064301 (2012); 10.1063/1.3682323

Spectroscopic study on the structural isomers of 7 -azaindole (ethanol) n (n = 1 – 3) and multiple-proton transfer reactions in the gas phase
J. Chem. Phys. **130**, 224307 (2009); 10.1063/1.3149772

A high-resolution pulsed field ionization-photoelectron-photoion coincidence study of vinyl bromide
J. Chem. Phys. **120**, 11031 (2004); 10.1063/1.1739402

Photoionization of cold gas phase coronene and its clusters: Autoionization resonances in monomer, dimer, and trimer and electronic structure of monomer cation

Philippe Bréchignac,[1,a)] Gustavo A. Garcia,[2] Cyril Falvo,[1] Christine Joblin,[3] Damian Kokkin,[3] Anthony Bonnamy,[3] Pascal Parneix,[1] Thomas Pino,[1] Olivier Pirali,[1] Giacomo Mulas,[4] and Laurent Nahon[2]

[1]*Institut des Sciences Moléculaires d'Orsay, CNRS UMR8214, Univ Paris-Sud, F-91405 Orsay, France*
[2]*Synchrotron SOLEIL, L'Orme des Merisiers, Saint-Aubin, B.P. 48, F-91192 Gif-sur-Yvette, France*
[3]*IRAP, Université de Toulouse 3 - CNRS, 9 Av. Colonel Roche, B.P. 44346, F-31028 Toulouse Cedex 4, France*
[4]*INAF - Osservatorio Astronomico di Cagliari, via della scienza 5, I-09047 Selargius (CA), Italy*

Polycyclic aromatic hydrocarbons (PAHs) are key species encountered in a large variety of environments such as the Interstellar Medium (ISM) and in combustion media. Their UV spectroscopy and photodynamics in neutral and cationic forms are important to investigate in order to learn about their structure, formation mechanisms, and reactivity. Here, we report an experimental photoelectron-photoion coincidence study of a prototypical PAH molecule, coronene, and its small clusters, in a molecular beam using the vacuum ultraviolet (VUV) photons provided by the SOLEIL synchrotron facility. Mass-selected high resolution threshold photoelectron (TPES) and total ion yield spectra were obtained and analyzed in detail. Intense series of autoionizing resonances have been characterized as originating from the monomer, dimer, and trimer neutral species, which may be used as spectral fingerprints for their detection in the ISM by VUV absorption spectroscopy. Finally, a full description of the electronic structure of the monomer cation was made and discussed in detail in relation to previous spectroscopic optical absorption data. Tentative vibrational assignments in the near-threshold TPES spectrum of the monomer have been made with the support of a theoretical approach based on density functional theory. © *2014 AIP Publishing LLC.*
[http://dx.doi.org/10.1063/1.4900427]

I. INTRODUCTION

Polycyclic aromatic hydrocarbons (PAHs) constitute a large chemical family among all organic compounds. Their chemical and electronic properties have long been studied using all available analytical tools[1,2] and rapidly evolving theoretical means,[3,4] resulting in published spectroscopic atlases.[5–8] The input from photoelectron data into photoabsorption spectroscopy has been early and deeply discussed for PAHs.[9,10] Today, large open access databases have been implemented for both infrared[11,12] and visible-UV spectral properties of this family of molecules.[12]

Over the past three decades, this rich class of molecules has received a renewed interest and a growing attention, in particular in both the combustion[13] and astrophysics[14] communities. On the one hand, PAHs are major products in incomplete combustion processes, with considerable implications for health and environmental issues.[15] On the other hand, since PAHs were first proposed in 1984[16,17] to account for the observation of infrared bands seen in emission toward astrophysical objects exposed to irradiation by the UV starlight,[14] their existence in interstellar space has also been invoked to account for the observation of other astrophysical signatures including the Diffuse Interstellar Bands (DIBs)[18,19] and the UV extinction bump at 217.5 nm[20–24] in the interstellar extinction curve. These astrophysical implications were recently reviewed.[14,25]

In both combustion and astrophysics, the interaction of PAH molecules with UV/vacuum ultraviolet (VUV) photons plays an important role, and the present basic knowledge on their photophysical properties is far from being satisfactory. In the astrophysical context, the photoproducts, such as radicals and ions, resulting from photoinduced reactions take part in the interstellar chemistry. For these reasons, gas phase spectroscopic and photodynamical studies of cold PAHs and their derivatives, cations in particular, in the UV-visible wavelength range, are strongly needed.

Resulting from the observations of the last few IR space missions (ISO, Spitzer, AKARI), it has been shown that free gas-phase PAHs are mainly observed at the surface of interstellar clouds that are exposed to the stellar UV radiation field and that these PAHs are – at least partly – produced by photo-evaporation of larger particles, often referred to as "nanograins."[26] The stellar UV flux is also responsible for the formation, through photoionization, of the cationic fraction of the PAH distribution. The exact nature of these nanograins is so far unclear, but PAH clusters have been proposed as possible models[27] for them. However, experimental data on these systems are very scarce[28] and do not provide quantitative

a)Author to whom correspondence should be addressed. Electronic mail: philippe.brechignac@u-psud.fr

values that can be used in astronomical models. In addition, the difficulty to describe the delocalization of the charge (or electronic excitation) in these large systems[29] makes theoretical simulations a real challenge.

In this context, the highly symmetric coronene molecule, $C_{24}H_{12}$, can be considered as a prototype. Therefore, we have recently started a systematic study of the vibrational and electronic spectra of the coronene cation and its clusters, in order to increase our knowledge of their electronic and structural properties, and potentially provide spectral fingerprints that could be used to identify these species in space. In this article, we report a study on the valence shell photoelectron spectroscopy of coronene, and its dimer and trimer where applicable, paying particular attention to the autoionization (AI) resonances found near their respective ionization thresholds.

The first information on the photoelectron spectrum of gas phase coronene was published in 1972.[30,31] It was obtained by classical photoelectron spectrometry using HeI excitation, in a study primarily aimed at the experimental determination of the first π-orbital energies. These results, as well as those obtained on a large set of PAHs, were soon after complemented by the same authors,[32] with a quite thorough discussion based on quantum chemical calculations. In particular, since coronene is, together with benzene and triphenylene, a salient example of the D_{6h} point-group molecules with degenerate electronic states, the role of Jahn-Teller (J-T) distortion in its ground ionic state was considered. It was explicitly anticipated that, due to the high rigidity of the $C_{24}H_{12}$ skeleton, the corresponding splitting should be smaller than 70 meV.[32] More recently, the value of the J-T stabilization energy has been calculated by Kato *et al.*[33] to be 60 meV.

Before the early 1970s, new experimental techniques to prepare radical cations or anions in solid cryogenic matrices had been developed and mastered in the Shida's laboratory.[34,35] It allowed the development of extensive visible-ultraviolet absorption spectroscopic studies of charged species, which were applied in particular to the PAH family.[5] Since the cation molecular orbitals are involved in both the photoionization process and in optical spectroscopy, several attempts to rationalize the results of the two experimental sources of information[9,10,36–38] have been subsequently developed.

A short section is devoted below to the experimental aspects of the present study. Then, the obtained results are described in detail and discussed, with emphasis on the autoionization resonances which have been found and characterized, not only in coronene monomer but also in its small clusters. The attention is first focussed on the coronene monomer autoionization signals, before describing the results concerning the autoionization resonances in the coronene dimer and trimer. The findings on the electronic structure of the monomer radical cation are then discussed in relation to the existing optical absorption data.

II. EXPERIMENTAL METHOD

Experiments have been performed on the VUV undulator DESIRS beamline,[39,40] at the French synchrotron radiation facility SOLEIL. A commercial sample of coronene (99% purity, Sigma-Aldrich) was directly placed into an in-vacuum stainless-steel oven specially designed to withstand high temperatures. The oven was heated at 340 °C and the vaporized coronene was subsequently mixed with 1.1 bars of Ar and expanded through a 50 μm nozzle inside the SAPHIRS molecular beam permanent endstation.[41] The carrier gas and the backing pressure were chosen to maximize the production of coronene dimer. The resulting cooled free jet was sampled through a profiled skimmer (2 mm-i.d. orifice) to form a molecular beam of coronene-seeded argon. Coronene molecules (or clusters) were subsequently ionized by the synchrotron radiation beam crossing the molecular beam at the center of the DELICIOUS2 imaging electron/ion coincidence spectrometer.[42] Briefly, DELICIOUS2 consists of a velocity map imaging (VMI) analyzer coupled in coincidence with a Wiley-McLaren time-of-flight (WM-TOF) spectrometer providing mass-filtered photoelectron or photoion images. The extraction field can be set so that electrons emitted by the coronene (and its clusters) within a chosen range of their kinetic energy (KE) can be collected. Two main types of scans of the photon energy have been made: in the first type the extraction field was adjusted so that all the photoelectrons were collected without any discrimination in their kinetic energy, thus providing a mass-selected total ion yield (TIY) spectrum; in the second one the field was set to a lower value to improve the kinetic energy resolution in the electron channel. In this mode, the velocity map photoelectron image is obtained for each mass. These images are then analyzed to yield the full photoelectron image at each wavelength, or the threshold photoelectron spectrum (TPES), depending on which range of electron energies is sampled.

A 200 gr/mm low dispersion/high flux grating was set on the monochromator so that a typical photon flux of 10^{13} photons/s within a 17 meV bandwidth (typical value at 8.5 eV) was available on the sample. Higher order synchrotron radiation from the undulator's high harmonics was filtered out using a gas filter[43] filled with 0.14 mbar of Kr to achieve high spectral purity in the 7-12 eV range. The Kr absorption line[44] $4p^5 5s(3/2) - 4p^6\ {}^1S_0$ was used to calibrate the monochromator grating to an absolute energy precision of 3 meV.

During each scan, photoelectron images and cation TOF spectra were recorded in coincidence during a chosen accumulation time for each value of the photon energy. After a mathematical treatment[45] (to recover the original Newton sphere of expanding charged particles from its 2-D projection), the photoelectron spectra (PES) for coronene and its clusters can be extracted for each scan point, with electron kinetic energy resolutions ranging from 40% to 4% for the slowest and fastest electrons within the 5 eV KE bandwidth.[46] All the data presented in this work have been corrected for false coincidences (background noise) and photon flux variations, which were recorded thanks to a dedicated photodiode (AXUV/IRD).

III. RESULTS AND DISCUSSION

A. The molecular beam content

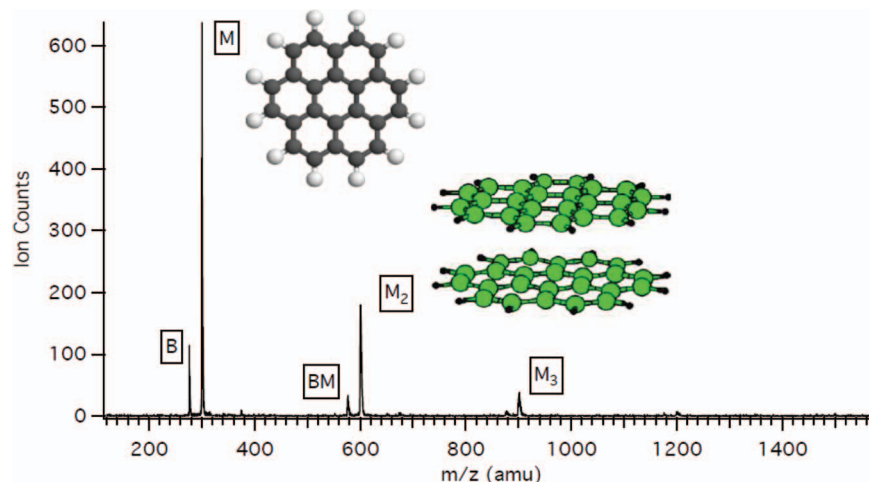Figure 1 shows the chemical composition of the coronene molecular beam, as measured by the WM-TOF of the

FIG. 1. TOF mass spectrum of the seeded coronene molecular beam recorded at $hv = 7.4$ eV. The M label corresponds to coronene monomer, while B represents the 1,12-benzoperylene, present as an impurity in the coronene sample. Dimers and trimers are present at a significant level. The molecular structures drawings correspond to the results of theoretical optimization.[47]

spectrometer at a fixed photon energy, $hv = 7.4$ eV. Coronene clusters up to the tetramer can be seen, plus satellite peaks corresponding to the presence of 1,12-benzoperylene as an impurity in the coronene sample. Note that, although the relative concentration of this species is enhanced in the gas phase as a consequence of its higher vapor pressure, its presence has no impact on the data since the coincidence treatment merely filters them out. In addition, the ^{13}C isotopomers distribution of the coronene monomer can be observed when zooming on the m/z = 300 peak, which places our mass resolution at about 300. Mass-selected photoion images have been recorded at various photon energies and have been used to extract the kinetic energy of coronene monomer and cluster cations. The analysis of the profiles of ion images confirmed that the data showed no evidence of fragmentation processes via dissociative ionization in the studied energy range, leading to the conclusion that all the masses in Figure 1 correspond to parent ions, i.e., ions which were formed by photoionization of the corresponding primary neutral species. Therefore, the spectra presented here correspond to pure size-selected targets. The ion images were also used to estimate a molecular beam temperature of 120 K from the kinetic energy distribution of cations. This temperature corresponds to the translational energy in the beam, and can be equated to the rotational temperature of the neutral species, the vibrational excitation being difficult to estimate since the degree of vibrational cooling may depend on the nature of each vibrational mode.

In Subsections III B–III E, the presented results always concern the coronene monomer, unless explicitly mentioned, like in Subsection III D 2 for the dimer and trimer.

B. Overview of the full monomer PES matrix

An overview of the electronic structure of the coronene monomer in the 7.1-10.1 eV region is shown in Figure 2, which allows the visualization of the PES plotted against the photon energy in matrix form, where a color code scale is used for the coincidence count rate.

The photon energy was scanned from 7.1 to 10.1 eV with a 7 meV step to encompass the region where autoionization resonances are observed. The extraction field for the electrons was set to collect all electrons whose kinetic energy is less than 4.7 eV, a value which is clearly larger than their maximum possible value when $hv = 10.1$ eV, since earlier work[30] locates the first ionization threshold near 7.3 eV. This PES matrix contains a wealth of information that can be reduced in several ways.

First of all, it provides the adiabatic ionization threshold – as the position of maximum count rate of the evident origin band – with an unprecedented accuracy (thanks to dedicated scans with a smaller step of 2 meV):
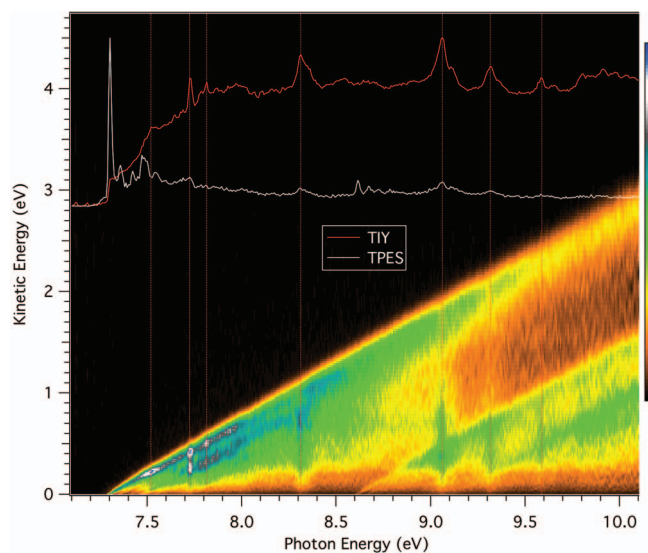

FIG. 2. Photoelectron spectral image, representing the count rate of electron/ion coincidences as a function of the photon energy hv (horizontal scale) and the electron kinetic energy KE (vertical scale). The mass channel corresponds to the coronene monomer cation. The top red trace corresponds to the TIY spectrum, as a function of hv, while the white trace corresponds to the TPES with an electron energy resolution $\varepsilon = 10$ meV. The main autoionization features listed in Table I have been marked with vertical dashed red lines.

IP = 7.310 ± 0.005 eV. It is in agreement with most previous photoelectron studies,[30,32,36] but the accuracy is improved by more than one order of magnitude. This value is slightly larger than the results obtained from photoionization efficiency measurements[48,49] in the threshold region, which are affected by temperature effects (hot tail), while measurements by electron impact ionization[50,51] suffer from a limited accuracy. Also plotted in Figure 2 is the TIY curve (red curve in the upper part of the figure). It is obtained by plotting the integral of the PES, over the full range of electron KE, as a function of the photon energy $h\nu$. Quite prominent along this total photoionization efficiency curve are bands peaking at intensity values which are clearly larger than that of the direct photoionization plateau. These features are due to AI resonances of the neutral molecule.

Since the kinetic energy of the electrons is analyzed for each value of $h\nu$ (vertical lines of the PES matrix), we are able, not only to ascertain the positions of the AI resonances, but also to determine for each resonance the distribution of final vibronic states of the cation toward which the resonant neutral state is decaying (see Subsections III C and III D). Finally, by plotting the integral of the slow electrons, $\int_0^\varepsilon PES(KE)\,dKE$ versus $h\nu$ (ε being chosen to a value close to the photon energy resolution), we extract the TPES (curve in white in the upper part of the figure) which provides the electronic structure of the cation bound states with an energy resolution of ε.

C. From TPES to photoionization yield (PIY)

Before commenting on the rich vibronic structure revealed by this TPES, punctuated by an intense adiabatic transition from the neutral to the cation ground state, we should look at Figure 2 in more detail. Indeed, it can be seen that some small features in the TPES appear as superimposed on the AI resonances seen in the TIY spectrum. This calls for a more careful look to the data, with the aim at sorting out the spectral features from the neutral or from ionic species.

One way to distinguish the cation transitions from the neutral AI resonances is to examine how the "TPES" curve evolves when increasing the upper limit of the integral over KE, which can be done from Figure 3. In the case of a cationic state, produced by direct ionization, whose energy is Ec_i, when $h\nu$ becomes larger than $(IP + Ec_i)$ the ion signal is expected to remain approximatively constant until another cationic state is encountered giving a steplike profile. Also the kinetic energy of the electron is uniquely given by the energy balance between the photon energy and the cation state energy (Ec_i): $KE = h\nu - (IP + Ec_i)$. On the contrary, in the case of a neutral AI state of energy E_{AIj} the ion signal is expected to rise then fall with a slope which depends on its spectral width and to peak exactly at the energy E_{AIj}. In addition, when a broader range of KE is admitted in the integral, the range of detected final cation states becomes larger, enhancing the total signal. This is illustrated in the panels (a) and (b) of Figure 3. In brief, the AI features increase in intensity with the KE bandwidth without changing their bandshapes, while direct ionization features evolve in shape from a TPES peak to a PIY step without change of their peak intensities.

Figure 3(a) covers the photon energy range from 7.2 to 8.7 eV. The direct ionization features are located between 7.3 and 7.8 eV, with autoionization features present above 7.44 eV. Two autoionization resonances are possibly superimposed on top of direct ionization peaks: a broad one centered near 7.52 eV and a narrow one located at 7.72 eV. Figure 3(b) covers the photon energy range from 8.5 to 10.0 eV. It reveals, for the low values of the KE bandwidth, the presence of at least 3 narrow peaks of direct ionization between 8.6 and 8.8 eV, while all the remaining features are due to AI resonances. These direct ionization peaks indicate the presence of an excited electronic state of the coronene cation in this spectral range. We will further discuss this point in Subsection III E 1 below.

D. Autoionizing resonances in the coronene monomer and clusters

1. Assignments in monomer: Analysis of the final states of the cation

Table I compiles the positions of some of the most prominent AI lines observed in this work, along with the values of their bandwidths, as extracted from the data presented in
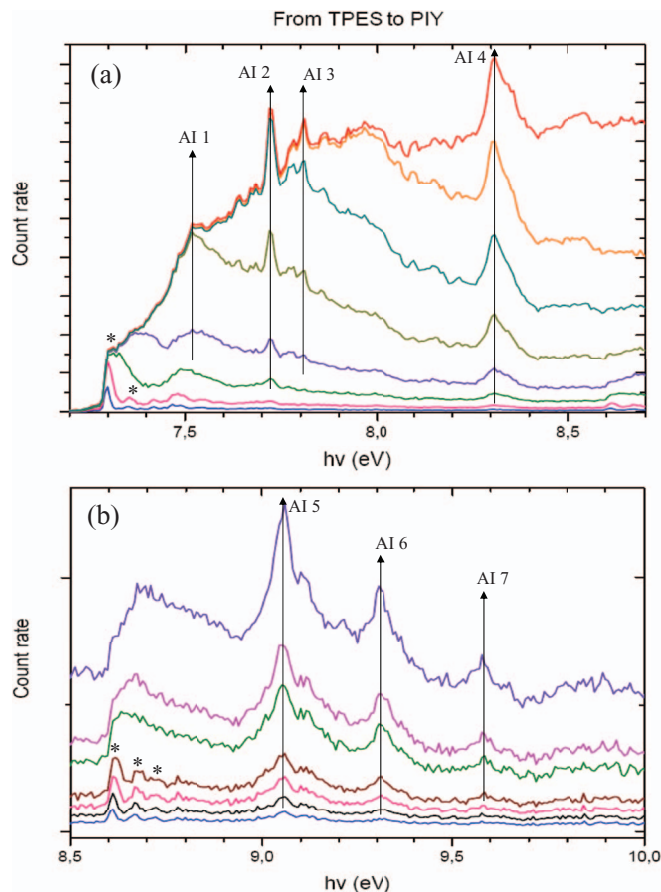

FIG. 3. Evolution of the "TPES" curve from $h\nu = 7.2$ to 8.7 eV (a) and from 8.5 to 10 eV (b) with the upper limit of the integral over KE. The different values of this limit are as follows. Panel (a): 0.004 eV, 0.015 eV, 0.052 eV, 0.12 eV, 0.28 eV, 0.5 eV, 0.78 eV, 3.11 eV; Panel (b): 0.004 eV, 0.008 eV, 0.015 eV, 0.025 eV, 0.052 eV, 0.07 eV, 0.12 eV. Asterisks mark the real TPES features, while arrows indicate the centers of AI resonances which are named according to their numbering in Table I.

Figure 3. It also lists the energies of the most probable final cation states resulting from their relaxation, obtained from the analysis of the photoelectron kinetic energy distributions when the photon energy is set, respectively, ON and OFF each resonance. Below 8.6 eV, all the AI resonant states decay toward either the ground adiabatic state of the cation, D_0 (v = 0) located at 7.310 eV, or to vibrationally excited states located above the adiabatic ionization limit, D_0 (v$\neq$ 0). As an example, Figure 4 shows the internal energy distribution of final cation states resulting from the excitation of two different AI resonances. Figure 4(a) corresponds to the narrow AI 2 peak at 7.724 eV, which shows three bumps that can be assigned, in order of decreasing probability to the v = 0 state, a vibrational state at 1370 ± 200 cm^{-1} and another at 2900 ± 200 cm^{-1}. With the accuracy of the positions being poor, these states could involve excitation of one and two quanta of a number of C–C stretching modes of the coronene cation skeleton. For the AI 4 resonance at 8.31 eV, the final cation state distribution peaks near 5800 cm^{-1}. Beyond 8.6 eV, the AI states primarily decay to other electronically excited states of the cation with a propensity to populate the highest energetically allowed vibronic states. This is apparent in Figure 4(b), in the case of the broad AI 6 resonance peaking at 9.312 eV.

As compiled in Table I, 7 AI resonances can be identified as members of a Rydberg series converging to 10.21 eV (see Figure 7(a)) and characterized by a quantum defect $\delta = 0.30 \pm 0.03$. The values of the principal quantum number n, extending from 3 to 9, are given in the fourth column of Table I. Considering the integrated absorbance (i.e., width × peak value) of these bands, their oscillator strengths are relatively large. This observation is consistent with the strength of the continuum associated with the excited cation state at 10.21 eV (see Subsection III E 2).

Concerning the bandshapes of these AI resonances, five of them exhibit quite broad bandwidths ($\simeq$ 60 meV, see the third column of Table I) as well as Lorentzian-like bandshapes, while only two (AI 2 and AI 3) are narrow enough to be significantly affected by the resolution of the beamline's monochromator. One can note that, from energy conservation and the electronic structure appearing in Table III below, these two resonances, as well as AI 4, can only relax to excited vibrational states of the cation ground electronic state, while other resonances, from AI 5 to AI 11, can relax to vibrational levels of excited electronic states.

Furthermore, it should be noted that some of the AI resonances seem to have an unresolved faint shoulder on the blue side of their profile, at an approximate distance of about 70 meV (see the complete TIY in Figure 5, with vertical lines marking the AI states). It may suggest excitation of a skeleton bending mode. But another possibility would be that these features would be members of a second Rydberg series converging toward the second J-T component of the above mentioned state at 10.21 eV, the approximate energy separation being consistent with the theoretical estimates of the J-T splitting.[32,33]

We note that the strongest AI resonances (4-5 bands presently reported within 8.31-9.81 eV) were present at low level in the VUV absorption spectrum of coronene vapor,
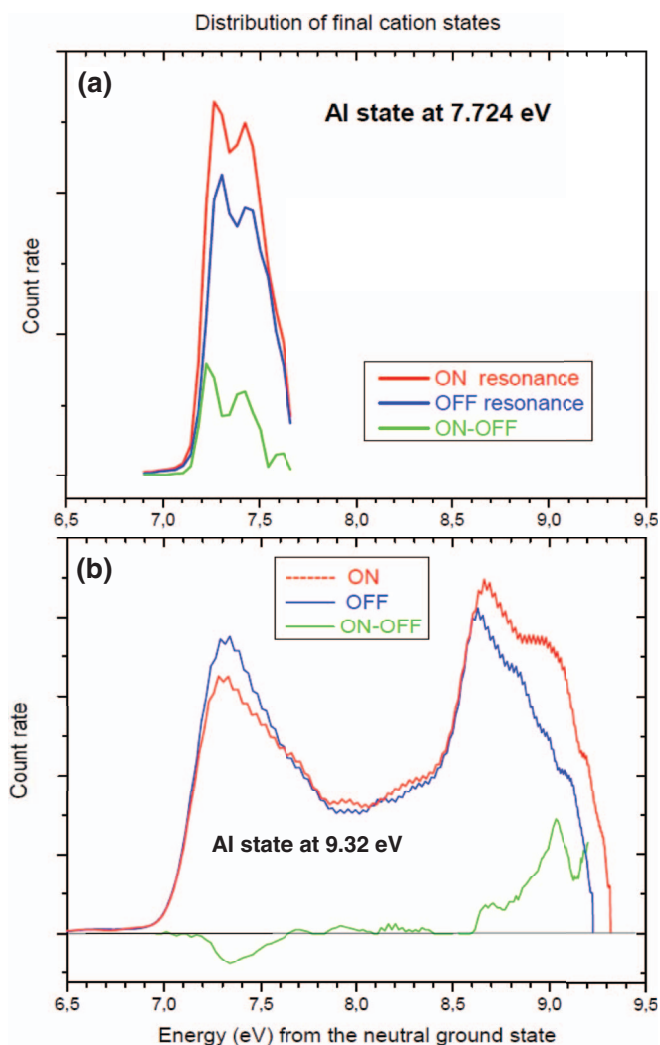

FIG. 4. Distribution of the final cation states resulting from the relaxation of the AI resonances in neutral coronene, derived from the photoelectron KE distribution. The statistics were improved by summing up the distribution of adjacent channels (columns of the PES matrix) corresponding to close values of the photon energy $h\nu$. 4 channels (28 meV) were used for panel (a) (narrow AI 2 feature) and 8 channels (56 meV) were used for panel (b) (broad AI 6 feature).

taken with a synchrotron radiation beam passing through an oven maintained at 530 K, by Joblin.[52]

It is worth emphasizing that low-n autoionization features are generally unexpected in large molecules such as coronene. Indeed, although the presence of autoionization states is undeniable, the high spectral density of vibronic states in these large molecules means that intra-molecular relaxation can efficiently compete with autoionization. However, coronene being a very stable, compact, and rigid molecule, its dynamical behavior under injection of internal energy probably differs from the usual case. It is interesting to observe that the loss of a (not so fast) electron becomes a preferred relaxation channel.

2. Autoionizing resonances in the coronene dimer and trimer: Spectral shifts from the monomer

As an introduction to this subsection, we recall that models of the interaction potential between a small number of

TABLE I. Peak positions in energy of the most prominent AI resonances of coronene monomer (found in this work). The n assignments (4th column) correspond to the values of the principal quantum number resulting from the identification of a Rydberg series (quantum defect $\delta = 0.30 \pm 0.03$) converging to the electronic excited state at 10.21 eV (see Figure 7(a)). The energies of the main final cation states (last column to the right) are derived from the comparison of the electron kinetic energy spectra recovered ON and OFF each resonance. The values in bold characters correspond to the dominant channels.

Band no	Position (eV)	Bandwidth (meV)	Rydberg n value	Electron KE (eV)	Final cation energy (eV)
AI 1	7.520	50	...	0.22	0.00
AI 2	7.724	20	...	**0.42**/0.25/0.06	**0.00**/0.17/0.36
AI 3	7.812	20	...	0.52/**0.34**	0.00/**0.18**
AI 4	8.310	60	3	0.70/**0.30**	0.32/**0.72**
AI 5	9.057	60	...	0.65/0.35/0.15	1.1/1.4/1.6
AI 6	9.312	60	4	0.6/0.3/0.1	1.4/1.7/1.9
AI 7	9.578	40	5	0.72	1.55
AI 8	9.802		6		
AI 9	9.907		7		
AI 10	9.970		8		
AI 11	10.026		9		

coronene molecules predict that the lowest energy cluster structures are sandwich-like, with a distance between molecular planes rather close to that of graphite. The coronene dimer was found to be a perfect twisted stack in which the two moieties share a common sixfold axis.[47,53] In addition, recent calculations by Rapacioli *et al.*,[54] using an extension of density functional based tight-binding (DFTB) methods which is adapted for molecular clusters, predict significant structural changes between the neutral and cation ground states: for instance, the intermolecular distance was found to be reduced from 3.35 Å in the neutral coronene dimer to 3.18 Å in the dimer cation, an effect that can primarily be interpreted as a result of charge resonance interaction.[54] Particular attention

will be paid in this subsection to the respective AI states of the two cluster systems (dimer and trimer) and how they compare to the case of coronene monomer.

Figure 6 displays a comparison of three spectra, respectively, obtained from the coincidence electron count rates relative to the mass channels 300 amu (monomer), 600 amu (dimer), and 900 amu (trimer) during the same scan of the synchrotron photon energy $h\nu$ from 7.0 to 10.5 eV. The kinetic energy bandwidth of the electrons was limited to $\varepsilon = 0.8$ eV, so that these curves represent partial ion yield spectra and not TIY. We focus here on autoionization features, while a more complete discussion of the photoionization spectra of coronene clusters will be the subject of future publications.
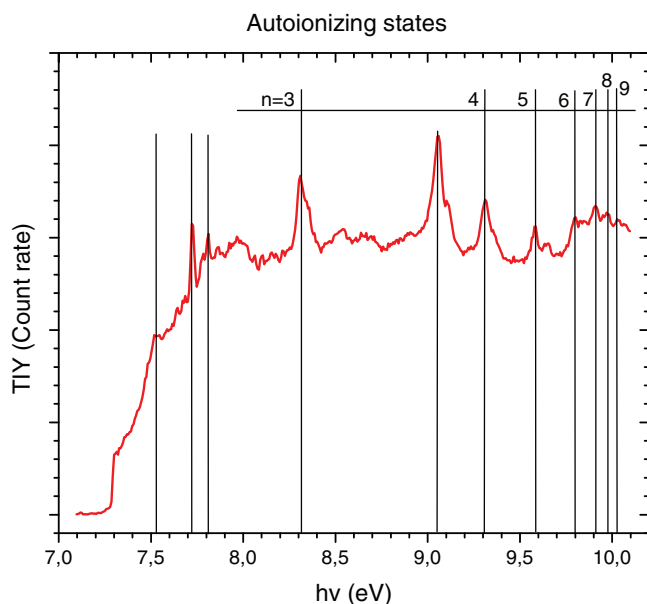

FIG. 5. Total ion yield spectrum of coronene monomer, in which the AI resonances have been marked by vertical lines. Positions in photon energy $h\nu$ are listed in Table I. The principal quantum number assignments are described by n values.
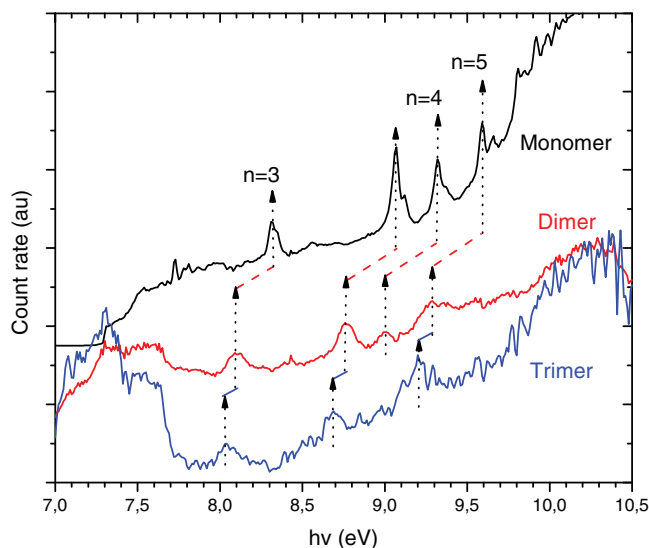

FIG. 6. Comparison of partial ion yield spectra of coronene monomer, dimer, and trimer with electron KE resolution $\varepsilon = 0.8$ eV. Scaling factors (5 for dimer, 50 for trimer) and vertical translations were used for better clarity. The cluster spectral shifts are emphasized: red segments from monomer to dimer and blue segments from dimer to trimer.

As mentioned for monomer at the end of Sub-section III D 1, it is remarkable that dimer and trimer also exhibit strong autoionization resonances despite the expected lifetime shortening due to the more efficient relaxation associated with their larger size. Vertical arrows pointing up have been added to help visualize these AI resonances. These arrows also allow to emphasize the cluster spectral shifts from monomer to dimer (red segments) and from dimer to trimer (blue segments) for the main peaks. Three of the dimer AI resonances have positions which are consistent with a Rydberg series assignment (see 4th column of Table II) characterized by a quantum defect $\delta = 0.32 \pm 0.03$ which converges toward an electronic state lying at 9.98 eV. This state was confirmed by the presence of a peak in the TPES spectrum, which will be discussed in a forthcoming paper. Only two Rydberg assignments are proposed in the case of the trimer cluster.

The main characteristics (positions, bandwidths, Rydberg assignments where applicable) of these new resonances are listed in Table II. Comparison of the second column of this table with that of Table I indicates that there is an approximately constant redshift in energy for the positions of the most prominent AI resonances, i.e.: the redshift is found within -0.27 ± 0.05 meV when going from the monomer to the dimer. Comparatively, the redshift from dimer to trimer is much smaller: -0.07 ± 0.01 eV. Note that, in case of Rydberg assignments, the n value of the Rydberg quantum number is conserved in the evaluation of these spectral shifts.

The final cationic states distribution resulting from the relaxation of the AI resonances is not as easy to extract as for the monomer, due to the broader nature of the clusters photoelectron spectra and to the lower signal-to-noise ratio. Nevertheless, we have attempted for two of the dimer bands (AI 1 and AI 3) to approximately locate the maximum in the electron kinetic energy distribution (see 5th column in Table II), and we can note that it remains small (clearly less than 1 eV).

The third column of Table II lists the bandwidths observed for the dimer, showing that they are about a factor of two larger than for the monomer (with the exception of AI 2). As mentioned in Subsection III D 1 for monomer, a vibrational and/or J-T contribution to this broadening should be considered in an appropriate theoretical description.

Finally, in comparing the data in Tables I and II, apart from the number of AI states, the main difference resides in the observed bandwidths, which take clearly larger values in the case of dimer. Among the reasons which may participate to explain this observation, one could invoke: (i) the vibrational congestion, with a much larger number of modes including some very low-frequency ones; (ii) the plausible existence of several conformers; (iii) the intracluster relaxation into vibrational excitation, whose rate is expected to increase with size; (iv) the dynamical migration of the electronic excitation from one monomer moiety to its neighbor resulting from dipole–induced dipole interaction. But we wish to also propose the role of the steric hindering, resulting from the just recalled "sandwich-like" dimer structure,[47] as a quencher of the Rydberg orbitals.

Indeed, the relatively small and consistent values of the quantum defect is probably in favor of p-like Rydberg orbitals, with their main axis perpendicular to the aromatic planes, which is similar to what was pointed out for the Rydberg states of benzene.[55] Assuming that Rydberg excitation within a dimer is, at a given time and without consideration of exciton-like hopping, centered relative to the geometric center of one monomer moiety, the presence of the second moiety at a distance (of the order of 3.4 Å) smaller than the classical Rydberg radius (4.8 Å for n = 3, 8.5 Å for n = 4, 13.2 Å for n = 5) is obviously a dramatic hindering for the electron motion. The lifetime associated with such states would thus be drastically reduced down to a few femtoseconds, as indicated by the bandwidths values.

E. TPES and vibronic structure of the monomer cation

The high resolution TPES spectrum represented in Figure 7(a) covers nearly the same internal energy range as the reference photoelectron spectrum of Boschi and Schmidt[30] recorded with a classical photoelectron analyzer and a He(I) lamp. Its dominant feature is the intense and narrow transition appearing at 10.21 eV, which marks the v = 0 vibrational level of an excited electronic state of the cation. Besides this transition, the already discussed AI features and the weak transition whose origin lies at 8.615 eV (with associated vibronic bands at 8.67 and 8.72 eV), a broad bump sits to the blue of the strong 10.21 eV band while the TPES signal rises again from 11.2 to 11.6 eV.

TABLE II. Peak positions in energy of the most prominent AI resonances of coronene dimer (left side) and trimer (right side). The n assignments (4th and 8th columns) correspond to the values of the principal quantum number resulting from the identification of two Rydberg series (quantum defect $\delta = 0.32 \pm 0.03$ for dimer, fixed at 0.33 for trimer) converging, respectively, to cationic excited states located at 9.98 eV for dimer and 9.86 $\pm$ 0.05 eV for trimer.

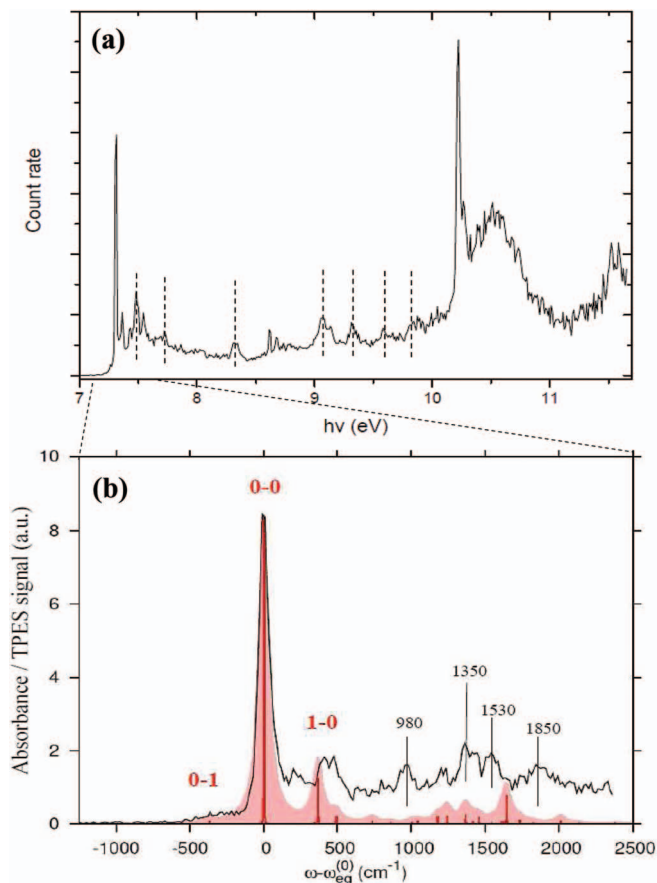| Band no Dimer	Position (eV)	Bandwidth (meV)	Rydberg n value	Electron KE (eV)	Band no Trimer	Position (eV)	Rydberg n value
AI 1	8.09	120	3	0.82	AI 1	8.03	3
AI 2	8.43	20	…		AI 2	8.7	…
AI 3	8.76	120	…	0.40	AI 3	9.21	5
AI 4	9.00	80	4				
AI 5	9.29	100	5				

FIG. 7. (a) Overview of the TPES spectrum of coronene monomer up to 11.7 eV; the positions of the main AI states are marked with dotted lines for clarity. (b) Close up of the cation ground state region (photon energy step 2 meV $\simeq$ 16 cm^{-1}, KE bandwidth 5 meV), compared with the theoretical prediction at 200 K (see text for details); contributions from AI 1 and AI 2 features have been subtracted; the red line shows a "stick spectrum" and the surface area in light red color its convolution with a 40 cm^{-1} Lorentzian lineshape (the relative position of the two spectra has been adjusted for matching on the 0-0 band).

1. The cation ground state: Comparison with theoretical predictions

Following the above assignments of AI resonances, it is now possible to distinguish in the low-KE spectrum of Figure 2 the cation states resulting from direct photoionization from the AI features. In order to make a detailed comparison of the present results with our theoretical predictions for the structure of the coronene cation ground state, we have built a corrected TPES spectrum by subtracting the contribution of AI resonances at 7.52 eV (AI 1) and 7.724 eV (AI 2) from the experimental TPES. This corrected TPES spectrum is shown in Figure 7(b) in the spectral window from 7.16 to 7.62 eV (i.e., -1230 cm^{-1} below to 2500 cm^{-1} above the 0-0 band).

The simulated TPES spectrum, also shown in Figure 7(b), was obtained from calculated "Franck-Condon" (FC) factors for the transition from the neutral ground state to the cation ground state (without consideration of the electron wavefunction nor of the vibronic interaction). These factors were computed using the linear coupling approximation, as described by Mukamel.[56,57] Similar to what was recently done for simulating the visible spectra of the 1- and

2-methylnaphthalene cations,[58] the two potential energy surfaces, as described by equilibrium geometries, harmonic frequencies, and normal modes, were obtained from DFT calculations with the B971-1 functional and TZ2P basis set.[59]

The symmetry of the equilibrium geometry of the neutral ground state was found to belong to the D_{6h} point-group, as expected. By contrast, the cation ground state equilibrium geometry was found to be of D_{2h} symmetry, as earlier found by Hirata *et al.*,[60] in agreement with the expected distortion due to J-T interaction.[33] To simplify the calculations, both neutral and cation were computed in D_{2h} symmetry. Only the 18 vibrational modes of A_g symmetry were found to carry FC activity, the largest coefficients being those of the modes at 368 cm^{-1}(45 meV) and at 1661 cm^{-1}(206 meV), and – at a lower level – the modes at 1262 cm^{-1}(156 meV) and 1377 cm^{-1}(171 meV). A list of vibrational frequencies for the 18 A_g modes and a graph of their FC coupling coefficients, as well as a sketch illustrating the atomic displacements involved by the ν_{18} vibration, can be found in the supplementary material[61] (Table SI and Figure S1).

The most prominent feature appearing in Figure 7(b) is the origin band marking the position of the adiabatic IP, also hinting at a very small geometry change between the neutral and the cationic species. Also interesting is the presence of a weak shoulder on the red side of the 0-0 band. Due to its variability with the jet expansion conditions (see Figure S2 in the supplementary material[61]), we assigned it to a hot band (0-1).

The simulated spectrum reproduces rather well this vibrationally excited state in the neutral as the A_g mode of energy 368 cm^{-1}, involving an in-plane deformation along the long symmetry axis (D_{2h}) (see the sketch of the atomic displacements in the supplementary material[61]). From the hot band relative intensity (ratio 0-1 to 0-0), the value of T_v $\simeq$ 200 K is derived for this particular mode. Although different vibrational modes will experience different degrees of cooling in the supersonic jet, we can nevertheless provide this temperature parameter as a rough estimate of the internal energy of the low frequency modes.

The overall agreement between the experimental and the theoretical spectra, without introduction of any adjustment factor, is – to some extent – satisfactory, although it is not the case when looking more carefully at the weak features. The four above mentioned modes, 368 cm^{-1} and 1661 cm^{-1} as well as 1262 cm^{-1} and 1377 cm^{-1}, find counterparts in the experimental spectrum, although the detailed vibronic structure of the photoionization transition appearing in the experimental spectrum does not precisely match the structure in the simulated spectrum. For instance, the 1-0 band, predicted at 368 cm^{-1}, is not completely clear in the experimental spectrum which peaks in that region at $\simeq$ 60 cm^{-1} above this value. The most probable reason for that can be attributed to the lack of an adequate description of the vibronic coupling resulting from the J-T interaction. In addition, the plausible presence of resonant autoionization processes occurring in this near-threshold region can also affect the relative intensities of particular TPES peaks. This relatively poor agreement will also impact the quality of the estimated temperature for the low frequency modes.

The vibrational J-T coupling constants reported by Kato *et al.*[33] favor three modes of E_{2g} symmetry (D_{6h}) at 496, 1013, 1668 cm^{-1}. Since E_{2g} species in D_{6h} point-group resolve into $A_g + B_{1g}$ species in the lower symmetry D_{2h} point-group, and the FC active modes are the A_g ones, a contribution from J-T active modes is expected in the FC distribution. While these last values bring a complement to the theoretical list (Table SI in the supplementary material[61]) of (FC allowed) frequencies, a detailed J-T analysis would be necessary to improve the comparison between experiment and theory. However, this would require a huge computational effort for such a large molecule, which is fully out of the scope of the present work.

Note finally that several high resolution UV wavelength scans were made in the region of the origin transition, from 7.1 to 7.9 eV. Depending on the exact beam conditions, the values of T_v for the coronene molecules in the beam were found between 200 and 350 K, which are significantly higher than the estimated translational temperature of the molecular beam.

2. Exploration of the excited electronic states of the coronene cation up to 11.6 eV

Considering the previous results obtained by conventional PES in the literature, it is quite surprising to see no trace of a state near 9.1 eV apart from the small satellite on the blue shoulder of the AI 5 resonance. Indeed, as early as 1972, Boschi and Schmidt[30] reported the experimental values of vertical IPs to be: 7.34, 8.64, 9.15, 10.4, 10.55, 11.8 eV. All these IP values have counterparts in our spectra, except for the ones at 9.15 eV and 10.4 eV (11.8 eV being out of the scanned energy range [see Figure 7(a)]). Note that a large uncertainty should be expected in the 10.4 eV value since this band was overlapped with the 10.55 eV one under a limited resolution.

Independent information about the excited electronic states of the coronene cation is indeed available, from the results of the near-IR and visible direct absorption spectroscopic studies in low temperature matrices.[5,62] It must be recalled that such studies are affected by the "matrix shift" resulting from the interaction of the cation with its solid environment, and this kind of shift is almost impossible to predict securely. Two main studies have been reported in the literature: the earlier one was conducted in a glassy organic matrix (Butyl chloride [BuCl]) by Shida and Iwata,[5] the second one in a Neon matrix by Ehrenfreund *et al.*[62] Caution must be taken when comparing the TPES data to that from absorption measurements for two main reasons: (a) strict selection rules apply in the latter case (absorption), but not in the former case (TPES); (b) absorption only involves configurations in the cation, while TPES involves both the neutral and cationic characteristics.

In addition to the aforementioned matrix-isolation studies, there has been a single study reporting the absorption spectrum of the coronene cation in the gas phase.[63] It consisted in the measurement of the laser-induced photofragmentation efficiency as a function of the laser wavelength in a cold Fourier transform ion cyclotron resonance (FT-ICR) trap. A relatively broad band, centered at 457 ± 1 nm ($\sim$ 2.71 eV, i.e., $\sim$ 10.02 ± 0.01 eV from the neutral ground state), was reported.

Both matrix studies reveal absorption bands at $h\nu$ = 1.75 eV and $h\nu$ = 1.82 eV, respectively, accompanied by a weaker feature separated by about 1600 cm^{-1} on the blue side. The difference in these positions is consistent with a difference in matrix shifts. From the position of the first IP at 7.31 eV, the electronic excited state involved in these transitions should be lying at 9.13 eV, in fair agreement with the old PES data. In the present data, this excited state should then be lying very close to the large autoionization resonance centered at 9.06 eV, making detection challenging due to the limited strength of the TPES signal. Nevertheless, the position of this state was confirmed by undertaking a mathematical transformation which selectively enhances the direct ionization events, as explained below.

Direct ionization events producing a cation of energy IE_i, where IE_i is the ionization energy of the ith state, will appear in the photoionization matrix along straight lines of constant slope $KE = h\nu - IE_i$ (which implies that $h\nu \geq IE_i$). Therefore, to amplify the signal of the direct ionization events, one can integrate the electron yield along this diagonal direction within a given electron kinetic energy range, following the expression:

$$PES(IE_i) = \int_{KE_{Min}}^{KE_{Max}} S((KE + IE_i), KE)\mathrm{d}KE,$$

where $S(h\nu, KE)$ is the photoionization intensity matrix shown in Figure 2. In this case, in spite of a reduced resolution, the signal from photon resonant events, such as autoionization ones, will be diluted due to the partial integration over the photon energy, while direct ionization events will be enhanced. Figure 8 shows the result of this analysis for an interval of $0.3 \leq KE \leq 0.5$ eV (a), along with the TPES (b) and TIY (c) curves for comparison. The third electronic band which was barely visible in the TPES curve and shadowed by a strong autoionization feature, is now visible as a weak
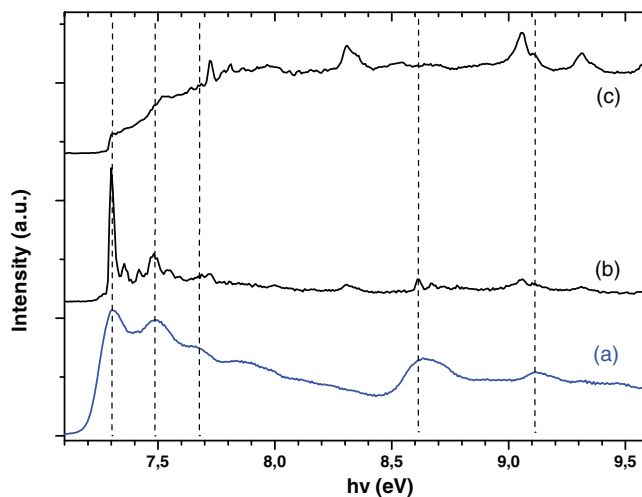

FIG. 8. (a) Result of the data treatment enhancing the intensity of cation electronic states while diluting that of AI neutral resonances (see text for details); (b) TPES; (c) TIY.

TABLE III. Adiabatic energies of the excited electronic states of coronene cation, relative to the neutral ground state and from the D_0 cation state. The second column recalls the values of the successive IPs measured by Boschi and Schmidt.[30] The assignments in terms of involved π molecular orbital (MO) are given in both D_{6h} and D_{2h} symmetry point-groups. Note the following exception: according to Deleuze,[4] the $1e_{2g}$ orbital for the D_4 state is of σ type. The values in columns 7-9 are taken from optical absorption studies. The last (right) column lists our new TD-DFT theoretical values. The numbers in bold characters correspond to the experimental values measured in the present work.

Energy (eV)	IP[30] (eV)	Label	MO (D_{6h})[32]	MO (D_{2h})[60]	ΔE from D_0 (eV)	BuCl[5] (eV)	Neon[62] (eV)	Gas[63] (eV)	E_{calc} (eV)
7.310	7.34	D_0	$2e_{2u}$	a_u or b_{1u}	0				0
8.615	8.64	D_1	$2e_{1g}$	b_{3g} or b_{2g}	**1.305**	1.30	1.31		1.21
8.67		$D_1(v_1)$			**1.36**				
8.72		$D_1(v_2)$			**1.41**				
9.11	9.15	D_2	$1b_{1g}$[4] or $1b_{2g}$	b_{3g} or b_{2g}	**1.80**	1.75	1.82		1.69
10.04	10.4	D_3	$2a_{2u}$	b_{1g}	**2.73**	2.60	2.70	2.71	2.61
10.21	10.55	D_4	$1e_{2u}$ or $1e_{2g}$[4]		**2.90**	2.89			2.91

transition centered at 9.11 ± 0.05 eV, along with the ground (7.31 eV) and first (8.615 eV) excited states, while the autoionization bands are washed out.

In summary, Table III presents the electronic/vibronic assignments of the coronene cation that have been achieved in this study. All the involved electronic states should correspond to ionization from π orbitals. We have indicated in this table the symmetry species of the involved molecular orbitals:

– in the 4th column, in the D_{6h} point-group: according to Boschi *et al.*[32] (for all the five states) and to Deleuze[4] (which differ only for the D_4 state), whose studies focussed on PES properties;
– in the 5th column, in the D_{2h} point-group (i.e., in the cation distorted geometry): following the study by Hirata *et al.*[60] which focussed on the absorption spectrum of the cation.

It is noticeable that the symmetry species listed in these two columns are consistent with the classical correlation rules for the resolution of the symmetry species when going from the D_{6h} point-group to the lower symmetry D_{2h} point-group, except for the D_3 state line where a_{2u} species (D_{6h}) should correlate with b_{1u} (D_{2h}). Note that Deleuze,[4] in a comparative study with OVGF/cc-pVDZ and TD-DFT calculations, suggested that the state at 9.11 eV (D_2) would be due to the $1b_{1g}$ π-orbital only, while the $1b_{2g}$ orbital would be lying at approximately 0.36 eV above the $2e_{1g}$ orbital. Nonetheless, nothing in the present experimental results allows us to confirm this suggestion.

Table III also recalls the results of the optical absorption studies which have been mentioned above, in which the photon energies of absorption bands are expected to correspond to differences between those of cation excited D_n states and the first adiabatic IP at 7.31 eV. This is actually the case for the four transitions $D_1 \leftarrow D_0$ to $D_4 \leftarrow D_0$. Note that this assignment is supported by the presence of two distinct bands between 2.5 and 3.0 eV in the optical absorption spectrum of the coronene cation in cold BuCl matrix,[5] while the three independent measurements of the $D_3 \leftarrow D_0$ transition are in fair overall agreement, even with considering

the role of matrix shifts. It follows that the IP value reported by Boschi and Schmidt[30] (second column) for D_3 is inaccurate, which can be understood considering the low resolution of their reported PES data. Note also that only two states (D_0 and D_4), among the five listed ones, were found to exhibit large photoionization cross sections in our experimental conditions.

It is expected from dipole selection rules that all the cation states optically connected to D_0 must be of "g" character. This is indeed the case with the previous orbital assignments for the D_1 and D_2 states. For the D_3 state, we suggest then that the involved MO should be b_{1g} (D_{2h}), rather than $2a_{2u}$ (D_{6h}). Conversely, the MO of the electron ejected to form the D_4 state should be issued from the $1e_{2g}$ (D_{6h}) σ-orbital, as proposed by Deleuze[4] (which resolves into a_g + b_{1g} in D_{2h} point-group), rather than from the $1e_{2u}$ (D_{6h}) π-orbital. It should be stressed that the complete interpretation of the electronic structure of the coronene cation appearing in Table III is in almost perfect agreement, within ± 0.13 eV, with the results of additional TD-DFT calculations of the first few vertical transitions in D_{2h} geometry. These calculations were done with TD-DFT, using the B-LYP exchange-correlation functional and the def2-TZVP basis set, with the resolution of identity approximation as implemented in the Turbomole code. The output listing indeed provided J-T pairs of states, whose splittings remain between 22 and 37 meV. Only average positions are listed in the last column of Table III.

As a final remark, it is interesting to note that the band at 10.04 eV, assigned to the D_3 state, is not directly observable in our TPES data, due to its low cross-section at threshold, and to the rich background coming from autoionization processes in this spectral region, with many members of the Rydberg series of neutral AI states converging toward the D_4 state at 10.21 eV. However, a weak shoulder appearing at that energy (10.04 eV) can be identified in the photoelectron spectra recorded at higher photon energies, which are given in the supplementary material.[61] This shoulder could be attributed to the D_3 state, but its low signal precludes an unambiguous assignment.

IV. CONCLUSION

The present study has reported new gas phase data on the photoionization spectroscopy of a model PAH of large size. These data represent the first detailed investigation on the electronic structure of coronene cation in the energy range between 7.0 and 11.7 eV above its neutral ground state. A number of autoionization resonances have been unexpectedly observed near the first adiabatic ionization threshold of coronene, its dimer, and its trimer, relaxing to both vibrationally and electronically excited cationic states. We have reported their positions and identified a long Rydberg series converging to the D_4 electronically excited state. In the monomer case, we have been able to pinpoint the final cationic states after the electronic relaxation by measuring the kinetic energy of the emitted electron, whereas the inherent lack of resolution in the dimer spectra leads to a more challenging or even impossible assignment of the final cationic state.

Due to the relatively long lifetimes of these autoionization features, the fact that the experimental technique does not introduce any other source of broadening apart from the spectral bandwidth admitted through the beamline monochromator, and their quite large cross sections, these bands could provide a solid laboratory reference for a possible future interstellar detection of these species. Consequently, the feasibility of a detection of coronene in the interstellar medium, based on this spectral fingerprint in the VUV spectral window, might be worth consideration. Similarly, it may be of interest to consider using these bands for monitoring the aggregation processes which are probably involved in the first steps of soot formation.

In addition, we have presented the TPES curve of the coronene monomer, and shown that it presents a rich vibronic structure in the explored energy range with an intense adiabatic transition at the first ionization threshold and an even stronger one lying at 10.21 eV. Two of the features clearly visible in the absorption spectra of the ion do not appear or do so weakly in the TPES. The theoretically simulated photoelectron spectrum of coronene in the threshold region is in partial agreement with the experimental TPES, allowing to point out the important role of the J-T effect in its ionic ground state. This TPES provides the first experimental data for its analysis.

[1]E. Clar, *Polycyclic Hydrocarbons* (Academic Press, London, 1964).
[2]E. Clar, *The Aromatic Sextet* (Wiley, London, 1972).
[3]J. Weisman, T. Lee, and M. Head-Gordon, Spectrochim. Acta A **57**, 931 (2001).
[4]M. Deleuze, J. Phys. Chem. A **108**, 9244 (2004).
[5]T. Shida and S. Iwata, J. Am. Chem. Soc. **95**, 3473 (1973).
[6]W. Karcher, S. Ellison, M. Ewald, P. Garrigues, E. Gevers, and J. Jacob, *Spectral Atlas of Polycyclic Aromatic Compounds* (Kluwer Academic Publishers, 1988), Vol. 2.
[7]L. Nakhimovsky, M. Lamotte, and J. Joussot-Dubien, *Handbook of Low Temperature Electronic Spectra of Polycyclic Aromatic Hydrocarbons* (Elsevier, Amsterdam, 1989).
[8]T. Shida, *Electronic Absorption Spectra of Radical Ions* (Elsevier, Amsterdam, 1988).
[9]E. Clar and W. Schmidt, Tetrahedron **31**, 2263 (1975).
[10]E. Clar and W. Schmidt, Tetrahedron **33**, 2093 (1977).
[11]C. Boersma, C. W. Bauschlicher, Jr., A. Ricca, A. L. Mattioda, J. Cami, E. Peeters, F. Sánchez de Armas, G. Puerta Saborido, D. M. Hudgins, and L. J. Allamandola, Astrophys. J. Suppl. **211**, 8 (2014).
[12]G. Malloci, C. Joblin, and G. Mulas, Chem. Phys. **332**, 353 (2007).
[13]H. Richter and J. B. Howard, Prog. Energy Combust. Sci. **26**, 565 (2000).
[14]A. G. G. M. Tielens, Annu. Rev. Astro. Astrophys. **46**, 289 (2008).
[15]C. Menzie, B. Potocki, and J. Santodonato, Environ. Sci. Technol. **26**, 1278 (1992).
[16]A. Léger and J. L. Puget, Astron. Astrophys. **137**, L5 (1984).
[17]L. J. Allamandola, A. G. G. M. Tielens, and J. R. Barker, Astrophys. J. Lett. **290**, L25 (1985).
[18]A. Léger and L. D'Hendecourt, Astron. Astrophys. **146**, 81 (1985).
[19]G. Van der Zwet and L. Allamandola, Astron. Astrophys. **146**, 76 (1985).
[20]C. Joblin, A. Léger, and P. Martin, Astrophys. J. **393**, L79 (1992).
[21]J. Weingartner and B. Draine, Astrophys. J. **548**, 296 (2001).
[22]*Astrophysics of Dust*, Astronomical Society of the Pacific Conference Series Vol. 309, edited by A. N. Witt, G. C. Clayton, and B. T. Draine (Astronomical Society of the Pacific, San Francisco, 2004).
[23]W. Duley, Astrophys. J. **639**, L59 (2006).
[24]G. Rouillé, M. Steglich, Y. Carpentier, C. Jäger, F. Huisken, T. Henning, R. Czerwonka, G. Theumer, C. Boerger, I. Bauer, and H. J. Knoelker, Astrophys. J. **752**, 25 (2012).
[25]C. Joblin and A. Tielens, *PAHs and the Universe: A Symposium to Celebrate the 25th Anniversary of the PAH Hypothesis: Toulouse, France, 31 May–04 June, 2010*, EAS Publications Series (European Astronomical Society EAS, EDP Sciences, 2011), Vol. 46.
[26]M. Rapacioli, C. Joblin, and P. Boissel, Astron. Astrophys. **429**, 193 (2005).
[27]M. Rapacioli, F. Calvo, C. Joblin, P. Parneix, D. Toublanc, and F. Spiegelman, Astron. Astrophys. **460**, 519 (2006).
[28]P. Bréchignac, M. Schmidt, A. Masson, T. Pino, P. Parneix, and C. Bréchignac, Astron. Astrophys. **442**, 239 (2005).
[29]M. Rapacioli and F. Spiegelman, Eur. Phys. J. D **52**, 55 (2009).
[30]R. Boschi and W. Schmidt, Tetrahedron Lett. **25**, 2577 (1972).
[31]R. Boschi, J. N. Murrell, and W. Schmidt, Faraday Discuss. **54**, 116 (1972).
[32]R. Boschi, E. Clar, and W. Schmidt, J. Chem. Phys. **60**, 4406 (1974).
[33]T. Kato, K. Yoshizawa, and T. Yamabe, J. Chem. Phys. **110**, 249 (1999).
[34]T. Shida and W. Hamill, J. Chem. Phys. **44**, 2375 (1966).
[35]T. Shida and W. Hamill, J. Chem. Phys. **44**, 4372 (1966).
[36]Z. Khan, Spectrochim. Acta A **44**, 313 (1988).
[37]Z. Khan, Spectrochim. Acta A **44**, 1125 (1988).
[38]Z. Khan, Spectrochim. Acta A **45**, 253 (1989).
[39]SOLEIL, 2014, for general information, see http://www.synchrotron-soleil.fr/portal/page/portal/Recherche/LignesLumiere/DESIRS.
[40]L. Nahon, N. de Oliveira, G. Garcia, J.-F. Gil, B. Pilette, O. Marcouillé, B. Lagarde, and F. Polack, J. Synchrotron Radiat. **19**, 508 (2012).
[41]M. Richard-Viard, A. Delboulbe, and M. Vervloet, Chem. Phys. **209**, 159 (1996).
[42]G. Garcia, H. Soldi-Lose, and L. Nahon, Rev. Sci. Instrum. **80**, 023102 (2009).
[43]B. Mercier, M. Compin, C. Prevost, G. Bellec, R. Thissen, O. Dutuit, and L. Nahon, J. Vacuum Sci. Technol. A **18**, 2533 (2000).
[44]K. Yoshino and Y. Tanaka, J. Opt. Soc. Am. **69**, 159 (1979).
[45]G. Garcia, L. Nahon, and I. Powis, Rev. Sci. Instrum. **75**, 4989 (2004).
[46]G. A. Garcia, L. Nahon, C. J. Harding, E. A. Mikajlo, and I. Powis, Rev. Sci. Instrum. **76**, 053302 (2005).
[47]M. Rapacioli, F. Spiegelman, D. Talbi, T. Mineva, A. Goursot, T. Heine, and G. Seifert, J. Chem. Phys. **130**, 244304 (2009).
[48]S. Tobita, S. Leach, H. Jochims, E. Illenberger, and H. Baumgärtel, Can. J. Phys. **72**, 1060 (1994).

[49] D. Schroder, J. Loos, H. Schwarz, R. Thissen, D. Preda, L. Scott, D. Caraiman, M. Frach, and D. Bohme, Helv. Chim. Acta **84**, 1625 (2001).

[50] E. J. Gallegos, J. Phys. Chem. **72**, 3452 (1968).

[51] S. Denifl, B. Sonnweber, J. Mack, L. Scott, P. Scheier, K. Becker, and T. Mark, Int. J. Mass Spectrom. **249**, 353 (2006).

[52] C. Joblin, "Spectroscopie de molécules aromatiques, test du modèle PAH en astrophysique," Ph.D. thesis (Université Paris-7, 1992), pp. 152–153.

[53] M. Rapacioli, C. Calvo, F. Spiegelman, C. Joblin, and D. Wales, J. Phys. Chem. A **109**, 2487 (2005).

[54] M. Rapacioli, A. Simon, L. Dontot, and F. Spiegelman, Phys. Stat. Sol. B **249**, 245 (2012).

[55] E. E. Koch and A. Otto, Chem. Phys. Lett. **12**, 476 (1972).

[56] S. Mukamel, *Principles of Nonlinear Optical Spectroscopy* (Oxford University Press, New York, 1995).

[57] S. Mukamel and D. Abramavicius, Chem. Rev. **104**, 2073 (2004).

[58] H. Friha, G. Féraud, T. Troy, C. Falvo, P. Parneix, P. Bréchignac, Z. Dhaouadi, T. W. Schmidt, and T. Pino, J. Phys. Chem. A **117**, 13664–13672 (2013).

[59] D. T. F. A. Hamprecht, A. J. Cohen, and N. Handy, J. Chem. Phys. **109**, 6264–6271 (1998).

[60] S. Hirata, M. Head-Gordon, J. Szczepanski, and M. Vala, J. Phys. Chem. A **107**, 4940 (2003).

[61] See supplementary material at http://dx.doi.org/10.1063/1.4900427 for the figure comparing the BuCl matrix absorption spectrum with PES spectra taken at photon energies $h\nu = 10.87$ and 11.6 eV.

[62] P. Ehrenfreund, L. D'Hendecourt, L. Verstraete, A. Léger, W. Schmidt, and D. Defourneau, Astron. Astrophys. **259**, 257 (1992).

[63] F. Useli-Bacchitta, A. Bonnamy, G. Mulas, G. Malloci, D. Toublanc, and C. Joblin, Chem. Phys. **371**, 16 (2010).